

windblown dust or perhaps tephra layers from nearby volcanoes and must originate in the snow accumulation zone. They dip upglacier as expected and occur close to, as well as at least 30 km from, the ice front. Some bands show small-scale concentration variations, which may be expected from deposition around sastrugi ("snow dunes") or within ripple troughs. Because of this and because they contain only very fine material in nearly uniform bands they are not considered to be Thule-Baffin moraines. The dust bands that crop out can be traced, and no offsets or folds were found. The bands are exposed farther down-glacier in valleys in the ice surface, as expected from faster flow between obstacles in the glacial bed. The continuity and form of the dust bands support our simple model for ice flow and indicate that the ice is in stratigraphic order.

The calculations suggest that this part of the ice sheet has been approximately steady for some 600,000 years, during a time when other glaciers waxed and waned dramatically. There is also probably a long stratigraphic record of ice exposed near the Allan Hills. What this ice and its contained air and impurities will reveal about past changes in climate, ice sheet flow, atmospheric composition, and volcanic activity is yet to be determined. Such a record is without parallel and is intermediate in character between the more detailed but shorter term ice core records and the coarser sea floor and palynologic records.

I. M. WHILLANS

Department of Geology and Mineralogy
and Institute of Polar Studies,
Ohio State University, Columbus 43210

W. A. CASSIDY

Department of Geology and Planetary
Science, University of Pittsburgh,
Pittsburgh, Pennsylvania 15260

References and Notes

1. E. J. Olsen, *Nature (London)* **292**, 516 (1981).
2. T. Nagata, in *Proceedings of the Second Symposium on Yamato Meteorites*, T. Nagata, Ed. (Memoirs of National Institute of Polar Research, Tokyo, Japan, 1978), special issue 8, p. 70.
3. I. M. Whillans, *J. Glaciol.* **18**, 359 (1977).
4. $A_c = 0.039$ m/year [measured in the central portion of the ice sheet (16); average value for entire accumulation zone is probably within a factor of 2 of this value]. $A_b = 0.06$ m/year [measured in the 10 km nearest the Allan Hills (17); probably within a factor of 2 of the average value for the entire ablation zone]. $\phi = 1.3$ [from (3), not critical for influx calculations]. Position of equilibrium line is 100 km on the basis of the limit of blue ice on Landsat images and is probably accurate to 50 percent. Drewry (18) shows a very short flow line for the ice leading to the Allan Hills. Our observations on slopes and the deformation of dust bands lead us to conclude that the flow line is hundreds of kilometers long, as we have modeled it. $Z = 0.6x^{3/4}$ with Z and x in meters [empirical fit to radio echo-determined ice thicknesses (10)]. For $x > 100$ km, $Z = 3400$ m. For $\dot{\epsilon}_{ys} = |dx/dt|_s/R$, $R = 100$ km, $Z = 3400$ m. For $x < 100$ km and $R = \infty$ for $x > 100$ km (R is

- radius of curvature of elevation contours for ice flowing in direction of maximum slope).
5. About 60 percent of the meteorites have been transported through the glacier. Concentrations are increased by 25 percent at the snout because of the third mechanism, the effect of which is much less important farther inland.
 6. G. S. Hawkins, *Astron. J.* **65**, 318 (1960).
 7. H. Brown, *J. Geophys. Res.* **65**, 1679 (1960).
 8. ———, *ibid.* **66**, 1316 (1961).
 9. D. W. Hughes, in *Solid Particles in the Solar System*, I. Halliday and B. A. McIntosh, Eds. (Symposium 90, International Astronomical Union, Paris, 1980), p. 207.
 10. H. T. Millard, *J. Geophys. Res.* **68**, 4297 (1963).
 11. F. Nishio, N. Azuma, A. Higashi, J. O. Annexstad, *Ann. Glaciol.* **3**, 222 (1982).
 12. A. J. Gow and T. Williamson, *J. Geophys. Res.* **80**, 5101 (1975).
 13. E. L. Fireman, L. A. Rancitelli, T. Kirsten, *Science* **203**, 453 (1979); J. C. Evans, and L. A. Rancitelli, *Smithson. Contrib. Earth Sci.* **23**

- (1980), p. 45; K. Nishiizumi, J. R. Arnold, D. Elmore, X. Ma, D. Newman, H. E. Gove, *Earth Plant. Sci. Lett.* **62**, 407 (1983).
14. D. J. Drewry, *Nature (London)* **287**, 214 (1980).
 15. I. M. Whillans, *J. Glaciol.* **24**, 15 (1979).
 16. J. M. Pailas, I. M. Whillans, C. Bull, *Ann. Glaciol.* **3**, 239 (1982).
 17. F. Nishio and J. O. Annexstad, in *Proceedings of the Fifth Symposium on Antarctic Meteorites*, T. Nagata, Ed. (Memoirs of National Institute of Polar Research, Tokyo, Japan, 1980), special issue 17, p. 1.
 18. D. J. Drewry, in *Antarctic Geoscience*, C. Craddock, Ed. (Univ. of Wisconsin Press, Madison, 1982), p. 947.
 19. We thank J. Bolzan, R. Hooke, D. Hughes, and M. van Heeswijk for helpful comments. Supported by NSF grants DPP-7821104A02 and DPP-7920824. Contribution 466 of the Institute of Polar Studies.

29 July 1982; revised 10 May 1983

Eccentric Ringlet in the Maxwell Gap at 1.45 Saturn Radii: Multi-Instrument Voyager Observations

Abstract. *The Voyager spacecraft observed a narrow, eccentric ringlet in the Maxwell gap (1.45 Saturn radii) in Saturn's rings. Intercomparison of the Voyager imaging, photopolarimeter, ultraviolet spectrometer, and radio science observations yields results not available from individual observations. The width of the ringlet varies from about 30 to about 100 kilometers, its edges are sharp on a radial scale < 1 kilometer, and its opacity exhibits a double peak near the center. The shape and width of the ringlet are consistent with a set of uniformly precessing, confocal ellipses with foci at Saturn's center of mass. The ringlet precesses as a unit at a rate consistent with the known dynamical oblateness of Saturn; the lack of differential precession across the ringlet yields a ringlet mass of about 5×10^{18} grams. The ratio of surface mass density to particle cross-sectional area is about five times smaller than values obtained elsewhere in the Saturn ring system, indicating a relatively larger fraction of small particles. Also, comparison of the measured transmission of the ringlet at radio, visible, and ultraviolet wavelengths indicates that about half of the total extinction is due to particles smaller than 1 centimeter in radius, in contrast even with nearby regions of the C ring. However, the color and brightness of the ringlet material are not measurably different from those of nearby C ring particles. We find this ringlet is similar to several of the rings of Uranus.*

Images of Saturn's rings obtained by the Voyager cameras showed several eccentric features, including an elliptical ringlet in an otherwise clear gap at about 1.45 Saturn radii (1, 2) which is now called the Maxwell gap. In addition, we now have occultation studies of this feature at several wavelengths. Voyager 1 carried out a microwave occultation with the dual-frequency spacecraft transmitter as a source and reception on the ground (3); on Voyager 2, the star δ -Scorpii was observed by the ultraviolet spectrometer (UVS) (4) and the photopolarimeter (PPS) (5) as it was occulted by the rings. We briefly discuss these observations and draw conclusions regarding (i) the size of the ring particles, (ii) the distribution of material within the ringlet, and (iii) the total mass. Derived quantities are compared with other ring features.

The most detailed Voyager images of ring C had resolution of about 5 to 7 km per line pair (1, 2). The photometric brightness and the optical depth from the

stellar occultation determine that the particle visible reflectivity is 0.26. This is indistinguishable from the surrounding material; we find no significant difference in particle color or particle albedo between this feature and surrounding C ring, in contrast with earlier reports (6).

The radio occultation experiment measured the rings' optical depth at wavelengths of 3.6 and 13 cm (3). Previous results have been limited to a resolution of about 15 km (the Fresnel zone size at the ring). It is now possible to partially remove the diffraction effects for selected parts of the rings by applying an inverse Fresnel transform to the signal (7). The improved resolution is on the order of 1 km, although the data shown below have been smoothed to 10 km resolution.

On Voyager 2, the UVS and PPS instruments simultaneously observed the occultation of δ -Scorpii (HD 143275, B0.5 IV) by the rings. The UVS measured the extinction due to the ring at 1125 Å with a spatial resolution of about

3.5 km. The normal optical depth is found after removing a small background signal (< 1 percent) induced by energetic electrons in Saturn's magnetosphere, and correcting for variations in spacecraft pointing (8). The PPS measured the extinction of δ -Scorpii at 2650 Å with successive points separated by about 100 m in distance from Saturn (5, 9). The PPS results for optical depth may be somewhat more uncertain than UVS results because the background counting level for the PPS instrument was large (~ 28 percent of the star brightness).

Preliminary comparisons of the occultation data revealed differences in the radial scales determined by the various investigators. Voyager 2 PPS and UVS observations were in agreement with each other, but the Voyager 1 radio science (RSS) and UVS were not consistent with Voyager 2 observations within the estimated uncertainties in spacecraft position and pointing knowledge. This problem has been corrected by attributing all of the discrepancy to the uncertainty in the location of Saturn's pole and solving for a new pole position. The new value of the pole brings all occultation observations into alignment within about 10 km for features believed to be circular (10).

Figure 1 provides a comparison between the PPS and UVS observations, where the PPS curve has been smoothed to an equivalent resolution of 1 km. The two observations agree over most of the region. We attribute the discrepancy near the core of the ringlet to systematic errors in the removal of the background intensity I_B , which are accentuated at the larger values of optical depth. This problem does not affect the fine structure of the curves shown or the details of the curves for optical depth $\tau \lesssim 1$, since the

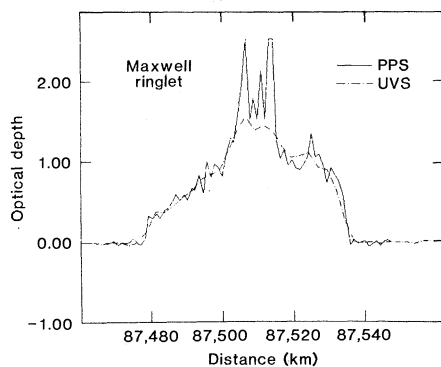


Fig. 1. Normal optical depth at wavelengths of ~ 1125 and 2640 Å from Voyager 2 stellar occultations. The resolution is 3.5 km at ~ 1125 Å (UVS) and 1.0 km at 2640 Å (PPS). The differences at large optical depth are probably exaggerated due to errors in removal of baseline intensity (see text).

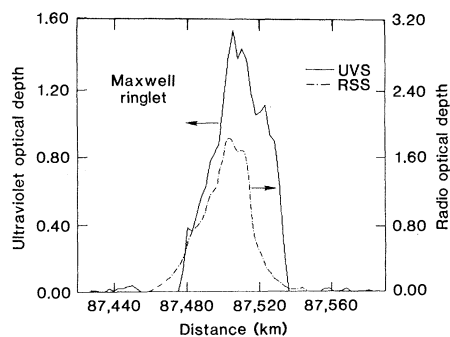


Fig. 2. The normal optical depth at wavelengths of 1125 Å and 13 cm from Voyager stellar and radio occultations. The radio curve has been scaled to the UVS width to compensate for difference in observing conditions (see text) and divided by two [see text and (12)]. The difference between the two profiles implies a significant population of centimeter-sized and smaller particles which are transparent at the longer wavelength.

curve is determined from $\ln(I - I_B)$, where I is the observed intensity.

At the resolution of Fig. 1 we can be quite certain about the structure of the ringlet. The Maxwell gap is entirely empty to the precision of the measurements. Upper limits on the average optical depth for 20 km on either side of the ringlet are $\tau < 0.011$ (UVS), $\tau < 0.009$ (PPS), and $\tau < 0.01$ (RSS; wavelength, 3.6 cm), while the optical depth in the surrounding parts of the C ring is 0.05 to 0.10 (4, 11). At the inner and outer edges of the ringlet the optical depth increases to a significant level in the span of a few hundred meters as observed by the PPS instrument (not shown), implying that these edges are sharp on the scale of 1 km in the PPS data. The central region of the ringlet contains an optically thick core about 15 km wide where the optical depth reaches a value of about 1.5 at 5 km resolution. This central core has two minor peaks in optical depth shown by both instruments. The actual sharpness and relative depth of the peaks are not well determined, however.

Additional information regarding the structure of the ringlet comes from the radio occultation of Voyager 1. As discussed below, the Maxwell ringlet does not have constant width: at the location of the radio observations its width was ~ 87 km, while at the time and location of the stellar occultations it was ~ 57 km. To compare these observations we assume that the ringlet is uniform, divide the radio occultation distance scale by the ratio of widths, and multiply the radio opacity by the same amount (Fig. 2). The coherent detection of the radio signal in the radio occultation is a significant difference between the two measurements (12). We correct for this dif-

ference by providing two different vertical scales in Fig. 2. In Fig. 2 we again see the suggestion of the narrow double peak in the central region of the radio data. Similar structure is seen also in the 3.6-cm results from the radio occultation (not plotted). This is evidence that, although the C ringlet changes in width, its overall morphology is stable.

The adjustment of vertical scales in Fig. 2 shows that the amount of ring material needed to produce the observed extinction is smaller at radio wavelengths. This difference implies that a substantial proportion of particles must be less than about 1 cm in radius (13). We estimate that about half of the cross-sectional area of the rings is in particles with typical radii less than 1 cm. To further quantify this, we assume that the particle size distribution is a power law with index -3 , with a maximum radius of ~ 3 m (14). To match both the PPS and radio observations the smallest particles must be about $30 \mu\text{m}$ in radius. For this distribution the number of particles smaller than 1 cm exceeds the number that are larger by a factor of 10^5 .

We now determine the shape and precession of this ringlet by comparison of these data with Voyager images. Prior to the occultation results, this ringlet was found to vary in width in the sense that the ring was narrower when closer to Saturn (1), similar to the behavior of ϵ ring of Uranus (15).

Lacking a comparably accurate distance scale for the Voyager images, we measure relative distances from the inner edge of the Maxwell gap. The observed width of the ringlet ranges from

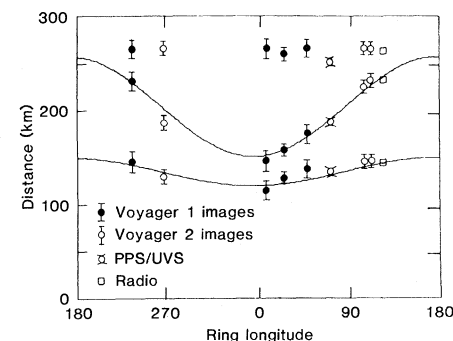


Fig. 3. Rectified measurements of ringlet shape. Three sets of points define the outer edge of the gap (top), the outer edge of the ringlet (central, with solid line), and the inner edge of the ringlet (lower, with solid line). The points have been rotated to Voyager 1 encounter epoch (17). The least-squares fit to the data gives the ringlet boundaries as $\rho_{\text{outer}} = (53 \pm 5) \sin(\phi - 85 \pm 12^\circ) + 204 \pm 5$ (km) and $\rho_{\text{inner}} = (15 \pm 5) \sin(\phi - 85 \pm 12^\circ) + 135 \pm 5$ (km), where ϕ is the longitude from the Voyager 1 subsolar point; solid curves are the best-fit curves.

about 38 km at its narrowest (several Voyager 1 imaging frames) to a maximum of 88 km (radio occultation and Voyager 2 imaging).

These measurements are corrected in longitude to the epoch of Voyager 1. Figure 3 shows all measurements, including points for which an accurate radial scale could not be determined, which were scaled to a constant gap width of 265 km (16). The observations were rotated to this epoch by using a precession rate of 14.66° per day, which was obtained by finding the least-squares fit of the Voyager 2 data to a sine wave initially fit to the Voyager 1 points, and assuming that the true precession rate was close to the theoretical rate of 14.68° per day (17) to resolve the multiple 2π ambiguity. It is clear from Fig. 3 that the expected precession rate is a satisfactory explanation of the data; if the precession differed by more than $\pm 0.04^\circ$ per day the fit to a sine curve is poor. The least-squares fit gives maximum and minimum ringlet widths of 107 ± 20 and 31 ± 20 km, respectively. The full variations in radius are 105 ± 10 and 30 ± 10 km for the outer and inner ringlet edges, respectively (18). We cannot rule out the possibility that the outer edge of the ringlet and the outer edge of the Maxwell gap are in contact.

For the ringlet to maintain an overall elliptical shape, some force must balance the differential precession due to the higher order moments of Saturn's gravitational field of orbits at different semi-major axes. One proposal is that apse alignment is maintained by self-gravity (19). A consequence of this assumption is that eccentricity should increase with semimajor axis, which in turn implies that the ringlet should be narrowest at pericenter, as seen.

This balance then determines the ring mass. We model the ring as N confocal, equal-mass ellipses equally spaced at quadrature in their orbits. We calculate the precession rate of each segment as the sum of an oblateness (J_2, J_4, J_6) term and a self-gravity term. The condition that the precession rates of all segments be equal yields a system of N equations in which the unknowns are the total mass of the ringlet, the value of the precession rate, and the eccentricities of the $N - 2$ interior ringlets. The eccentricities of the inner and outer boundary segments are fixed at the observed values. This model is clearly an approximation as the variation in optical depth across the ringlet strongly suggests a variation in mass of the individual segments.

This calculation gives a ring mass of 5×10^{18} g by extrapolating to an infinite

number of equal mass segments. The actual numerical computations had as many as 81 segments. The assumed constant opacity profile probably results in an overestimate of the mass by about 10 percent, based on similar computations for Uranus (19). However, other physical effects, such as the presence of small electrostatic potentials on the particles, could markedly alter our mass estimate. Note also that we ignore any gravitational effect from ring material surrounding the gap. This contribution should be small.

A physical parameter of interest is the ratio κ of optical depth in the visible to the surface mass density, referred to as the specific opacity. An average of the UVS and PPS occultation optical depth over the ringlet is $\langle \tau \rangle \approx 0.9$, giving (for width 57 km)

$$\kappa \approx 5 \times 10^{-2} \text{ cm}^2/\text{g} \quad (1)$$

This value is about five times larger than that determined from a similar analysis based on density waves in the B and A rings and Cassini division (5, 8, 11, 20, 21). The higher value of the specific opacity independently implies smaller particles in this ringlet relative to the other locations, in agreement with the inference from Fig. 2. In fact, the size distribution given above to explain the differences in optical depth between ultraviolet and radio wavelengths (power law with index -3 ; largest particle, 3 m; smallest particle, 30 μm) predicts

$$\kappa = 3 \times 10^{-2} \text{ cm}^2/\text{g} \quad (2)$$

The closeness of this calculated value to the measured value (Eq. 1) shows quantitative agreement between the inferred particle size distributions from these two independent observations.

The ringlet in the Maxwell gap may provide an analog for some of the rings of Uranus. Like the ϵ , α , and β rings, it is eccentric, with focus at the planet's center of mass, and precessing; like the η ring, it shows double-peaked structure. However, an obvious difference is that the double-peaked Uranian rings have their peak opacity just at the edges.

Our conclusions concerning the eccentric ringlet at $1.45 R_S$ are: (i) it lies in an otherwise empty gap in the C ring ~ 265 km wide; (ii) its width varies between 31 and 107 km, yet maintains sharp edges on the scale of 1 km; (iii) it has a double-peaked central core 15 km wide, with visual optical depth 1.5 to 2.0; (iv) the ringlet particles have color and albedo similar to those in the surrounding C ring; (v) the ringlet precesses at the rate expected due to the gravity field of Saturn; (vi) it has a total mass of about

5×10^{18} g and a specific opacity of $5 \times 10^{-2} \text{ cm}^2/\text{g}$, significantly larger than values obtained in other parts of the ring; and (vii) consistent with this large specific opacity, more than half of the ring cross section is due to particles in the ringlet with radii less than 1 cm.

L. W. ESPOSITO

Laboratory for Atmospheric and Space Physics, University of Colorado, Boulder 80309

N. BORDERIES

P. GOLDBREICH

Division of Geophysics and Planetary Science, California Institute of Technology, Pasadena 91125

J. N. CUZZI

NASA Ames Research Center, Moffett Field, California 94035

J. B. HOLBERG

Earth and Space Science Institute, University of Southern California, Tucson, Arizona 85767

A. L. LANE

R. B. POMPHREY

R. J. TERRILE

Jet Propulsion Laboratory, Pasadena, California 91109

J. J. LISSAUER*

Astronomy Department and Mathematics Department, University of California, Berkeley 94720

E. A. MAROUF

G. L. TYLER

Center for Radar Astronomy, Stanford University, Stanford, California 94305

References and Notes

1. B. A. Smith *et al.*, *Science* **212**, 163 (1981).
2. B. A. Smith *et al.*, *ibid.* **215**, 504 (1982).
3. G. L. Tyler *et al.*, *ibid.*, p. 553.
4. L. W. Esposito, J. P. Dille, J. W. Fountain, *J. Geophys. Res.* **85**, 5948 (1980); B. R. Sandel *et al.*, *Science* **215**, 548 (1982).
5. A. L. Lane *et al.*, *Science* **215**, 537 (1982); L. W. Esposito *et al.*, *J. Geophys. Res.* (special Voyager Saturn issue), in press.
6. An early report on photometry of the Maxwell ringlet indicated that its color was markedly different from the surrounding material (2). This finding was in error as a result of uncorrected differential smearing of the various images used to create the color composite.
7. E. A. Marouf and G. L. Tyler, *Science* **217**, 243 (1982); G. L. Tyler *et al.*, *Icarus* **54**, 160 (1983).
8. J. B. Holberg, W. T. Forrester, J. J. Lissauer, *Nature (London)* **297**, 115 (1982).
9. C. F. Lillie *et al.*, *Space Sci. Rev.* **21**, 159 (1977).
10. The new location of Saturn's pole is $\alpha_{1950} = 38.409^\circ \pm 0.016^\circ$, $\delta_{1950} = 83.324^\circ \pm 0.002^\circ$ (R. A. Simpson, G. L. Tyler, J. B. Holberg, *Astron. J.*, in press).
11. L. W. Esposito, M. O'Callaghan, R. A. West, *Icarus*, in press.
12. For particles roughly larger than the wavelength of observation, the effective size of a scattering particle is twice its physical cross section. This follows from the fact that as much light is diffracted by the particle as is physically blocked [H. C. van de Hulst, *Light Scattering by Small Particles* (Dover, New York, 1981)]. In radio occultation, the diffracted (scattered) wave is Doppler-shifted over a wide frequency band; thus, in the spectrum of the received signal, it can be separated from the narrow spectral line representing the reduced incident wave [G. L. Tyler *et al.*, *Icarus* **54**, 160 (1983)]. The extinction measured, therefore, reflects the fact that forward-diffracted energy is actually energy removed from the incident wave. On the other

hand, it is not always possible for an incoherent detector to distinguish the diffracted photons from those that are unscattered [J. N. Cuzzi and J. B. Pollack, *ibid.* 33, 233 (1978)]. If the particles are large compared to the instrumental aperture, the UVS and PPS instruments do not have the angular resolution to separate the direct and diffracted waves. In this case, diffracted photons appear unscattered and the extinction measured by the stellar occultation is half the extinction measured in the radio. The rough numerical equality of the microwave and optical extinctions implies that about half of the cross-sectional area effective in reducing the starlight is in centimeter-sized and smaller particles. The vertical scales in Fig. 2 have been adjusted to reflect this difference.

13. For a discussion of the dependence of extinction efficiency on wavelength, see J. E. Hansen and L. D. Travis, *Space Sci. Rev.* 16, 527 (1974).
14. E. A. Marouf *et al.*, *Icarus*, 54, 189 (1983).
15. J. L. Elliot *et al.*, *Astron. J.* 86, 444 (1981).
16. Uncertainties in the absolute scales of the imaging data made this procedure necessary for five points.
17. Theoretical precession calculated for mean radius of 87,500 km and J_2, J_4, J_6 from G. W. Null *et al.* [*Astron. J.* 86, 456 (1981)].
18. Measurements of the ringlet shape and precession could not be obtained independently. Figure 3 was obtained by rotating all Voyager 1 measurements to the epoch of Voyager 1 closest approach, using the theoretical precession rate

associated with measured values of J_2, J_4, J_6 . These corrections are $\sim 10^\circ$. The best-fit sinusoid to the Voyager 1 data on the outer edge was then determined. The Voyager 2 data were then corrected for differential rotation between Voyager 2 measurements, again $\sim 10^\circ$, and all Voyager 2 data rotated together to give the best fit with the previously determined Voyager 1 curve. This rotation corresponds to 14.66° per day if the ambiguity in the total number of rotations is resolved by use of the approximately 11.7 rotations obtained from the theoretical value. Voyager 1 images provide sufficient information to determine the total number of rotations as between 10 and 13. Best-fit sine waves to the corrected data were then determined for both the inner and outer edges of the ringlet, constrained to have the same phase.

19. P. Goldreich and S. Tremaine, *Astron. J.* 84, 1638 (1979).
20. J. B. Holberg, *ibid.* 87, 1416 (1982).
21. J. N. Cuzzi, J. J. Lissauer, F. H. Shu, *Nature (London)* 292, 703 (1981).
22. This work was supported by the National Aeronautics and Space Administration and by the Voyager Project. We thank S. Dermott, J. Elliott, F. Franklin, and P. Nicholson for helpful comments.

* Present address: Space Science Division, NASA Ames Research Center, Moffett Field, Calif. 94035.

5 April 1983; revised 6 July 1983

Neuron-Glia Adhesion Is Inhibited by Antibodies to Neural Determinants

Abstract. *Suspensions of embryonic chick neuronal cells adhered to monolayers of glial cells, but few neurons bound to control monolayers of fibroblastic cells from meninges or skin. Neuronal cell-glia cell adhesion was inhibited by prior incubation of the neurons with Fab' fragments of antibodies to neuronal membranes. In contrast, antibodies to the neural cell adhesion molecule (N-CAM) did not inhibit the binding. These results suggest that a specific adhesive mechanism between neurons and glial cells exists and that it is mediated by CAM's that differ from those so far identified.*

Interactions between neuronal and glial cells are believed to be of fundamental importance both in the development of the nervous system and in the mechanical and biochemical support of adult neural tissue (1). Neurites migrate over great distances by mechanisms that are believed to be dependent on glial cells for guidance and support (2), but the mechanisms responsible for these phenomena remain unknown. For example, Müller fibers in the retina and Bergmann glial fibers in the cerebellum have a long fibrous morphology spanning several cell layers and are closely associated with what appear to be migrating neurons (1). The search for molecules that might mediate such neuronal-glia interactions requires a specific assay, the development of which is reported below.

Previous studies on cell adhesion have concentrated mainly on homotypic cell adhesion, that is, the binding between similar or identical cells. For example, cell aggregation studies (3) have resulted in the isolation of distinct cell surface glycoproteins of different specificities called neural cell adhesion molecule (N-CAM) and liver cell adhesion molecule

(L-CAM); these molecules mediate, respectively, homotypic adhesion between neuronal cells and between liver cells (4). The study of the molecular basis of cell-cell adhesion between differing cell types (heterotypic cell adhesion) cannot, however, be accomplished unambiguously in vitro with an aggregation assay but must rely on techniques in which specifically identified cells of each type interact in a pairwise manner (5-8). Moreover, the methodology must ensure that such interactions be potentially distinguishable at the molecular level from homotypic interactions among cells of each type.

The binding of cells in suspension to cells in a monolayer has been used to measure adhesion between homologous and heterologous cell types (6, 8). In the case of N-CAM in particular, both homotypic (neuron-neuron) and heterotypic (neuron-myotube) forms of cell adhesion have been observed; in both cases, adhesion was specifically inhibited by Fab' fragments of antibodies to N-CAM (4, 8). The relevance of such assays as models for physiological cell-cell adhesion has been demonstrated by a number

of studies on N-CAM adhesion in more complicated experimental systems including histogenesis of the retina, neuronal fasciculation, and nerve-muscle adhesion (8, 9). In our present study, we have used such a heterotypic cell-cell binding assay to investigate the initial adhesion between neuronal and non-neuronal cells, focusing particularly on neuron-glia binding. Neuronal cells were found to bind specifically to glial cells and antibodies to neuronal cell surface determinants inhibited neuron-glia adhesion.

Single cell suspensions of neuronal cells were prepared from embryonic chick brain and retinal tissue in media free of Ca^{2+} and Mg^{2+} ions. The majority of these cells (85 to 90 percent) were identified as neurons on the basis that they contain N-CAM (4), a nerve-specific protein in cells from these chick tissues (10). Flat nonneuronal cells were purified from cell suspensions of neural tissues by their ability to adhere preferentially to collagen-coated substrates (11). These flat cells were obtained in culture free of neuronal cells, had a morphology that was typical of glial cells but different from fibroblasts (Fig. 1, a and c) (7, 11), and were not recognized by indirect immunofluorescence with the use of either monoclonal or polyclonal antibodies to N-CAM. Moreover, we have raised a monoclonal antibody that recognizes these flat cells in culture; it did not stain neurons and fibroblasts, and it stained astroglial-like cells in tissue sections by indirect immunofluorescence (12). These results strongly support the suggestion of others that the flat nonneuronal cells obtained from brain by similar procedures (11) are astroglia. It should be noted, however, that no completely satisfactory set of criteria is currently available for the recognition of chick astroglia in culture.

The extent of binding of fluorescently labeled neuronal cells in suspension to monolayers of forebrain glial cells during a 25-minute incubation period was much greater than the rate of binding to monolayers of fibroblasts (Fig. 1). No significant difference was detected in the adhesive specificity of neurons from brain or retina to monolayers of forebrain glia (Table 1, upper part). Embryonic glial cells from several parts of the central nervous system bound neurons in significant numbers. In contrast, other types of cells in monolayers, including those from the meninges, bound few cells. Neuronal cell binding was routinely performed in the absence of Ca^{2+} and the level of binding to glial cell monolayers was not significantly higher in the presence of